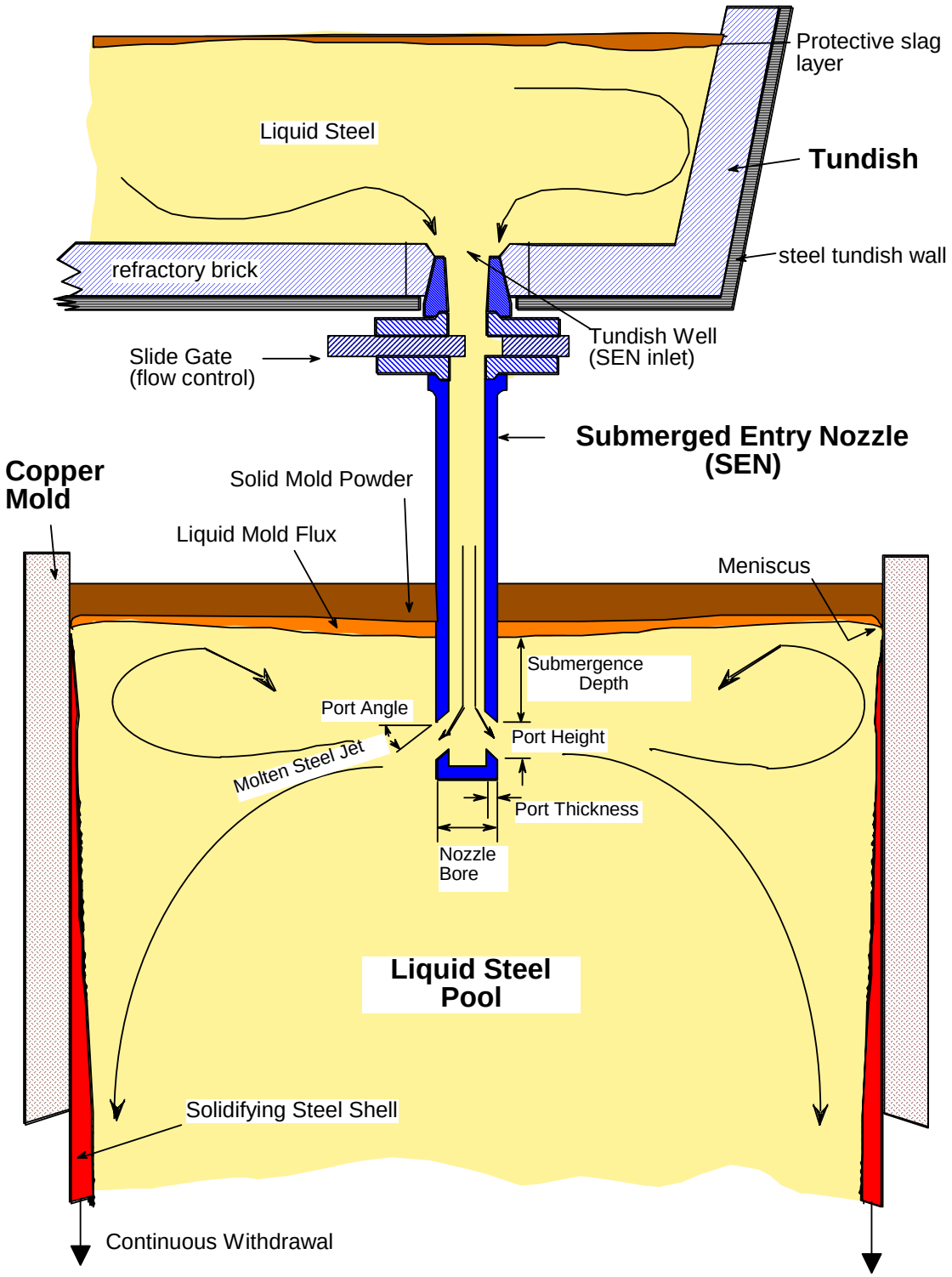

Fig. 1 Schematic of continuous casting process showing tundish, submerged entry nozzle, and mold

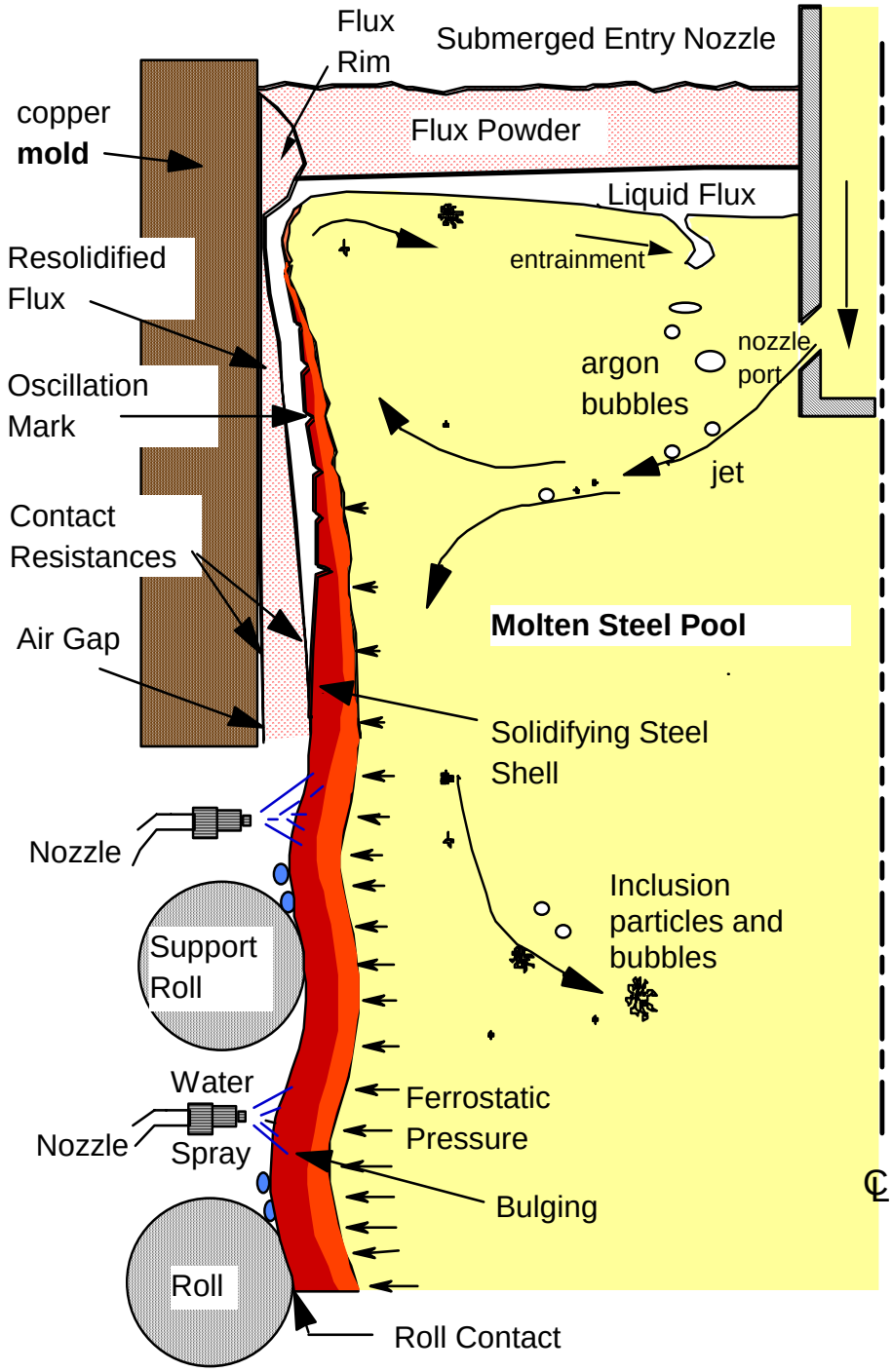

Fig. 2: Schematic of flow phenomena in mold region of continuous casting process.

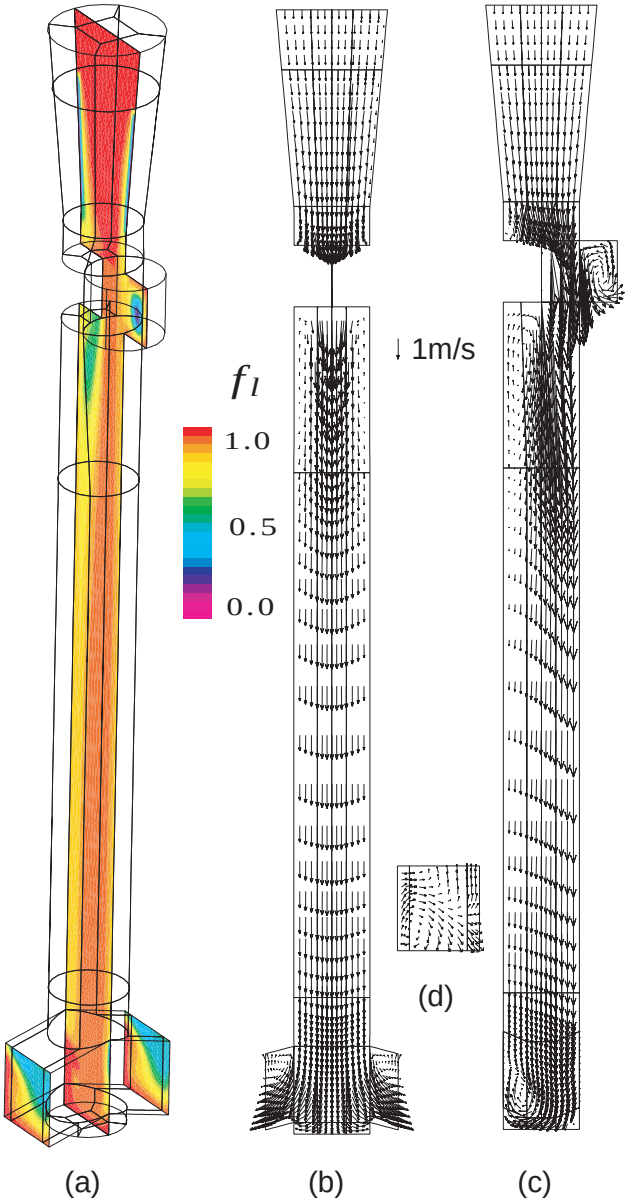

Fig. 3 Simulated flow field for the standard nozzle and conditions in Table I
(a) Argon gas distribution (b) Velocities in center plane parallel to WF
(c) Velocities in center plane parallel to NF (d) Velocities at port outlet plane

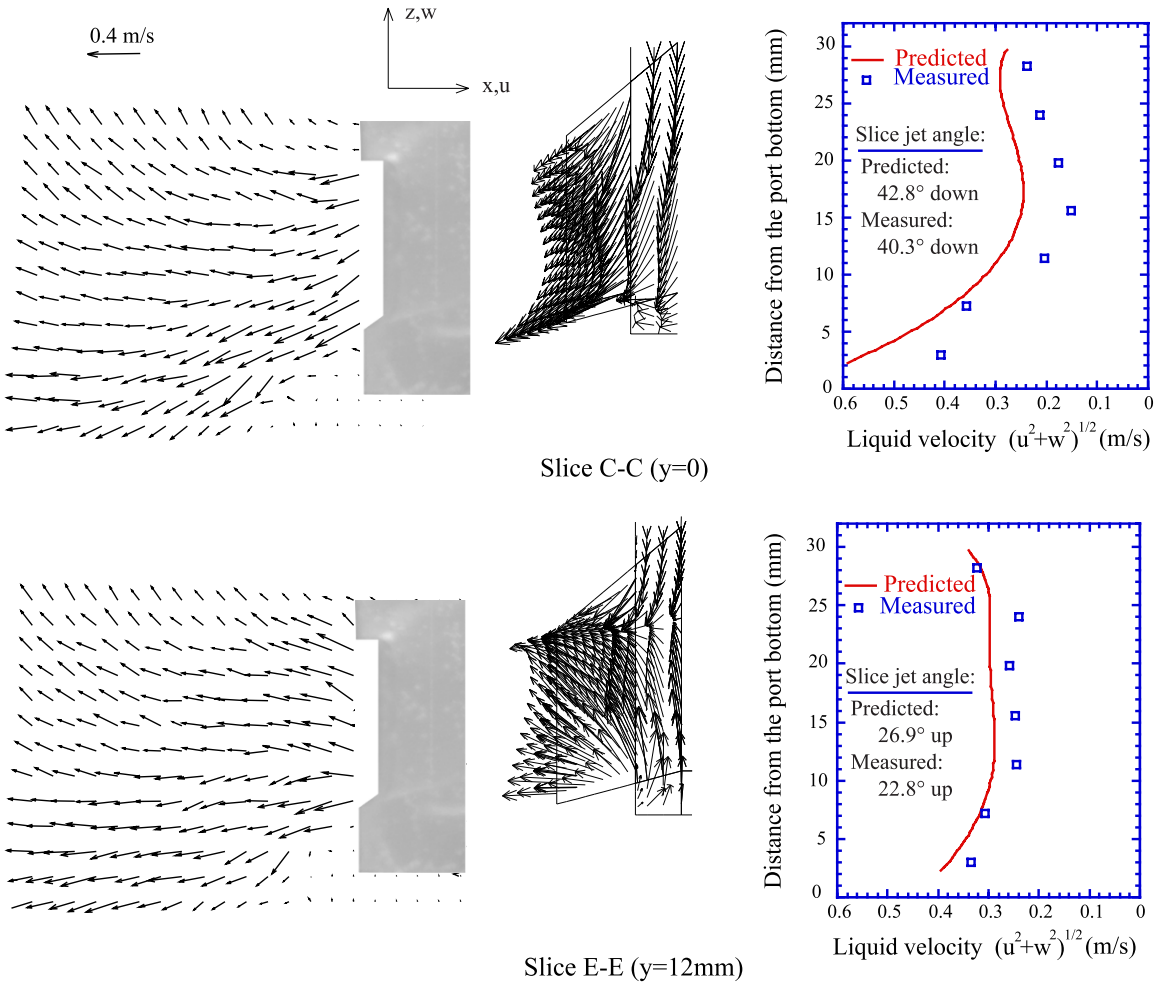

Figure 4 Comparison of PIV measurements and model predictions (0, 12mm from center plane of the nozzle, parallel to wide face of the mold) (a) PIV measurements (b) CFX predictions (c) magnitude comparison of PIV measurements and CFX predictions

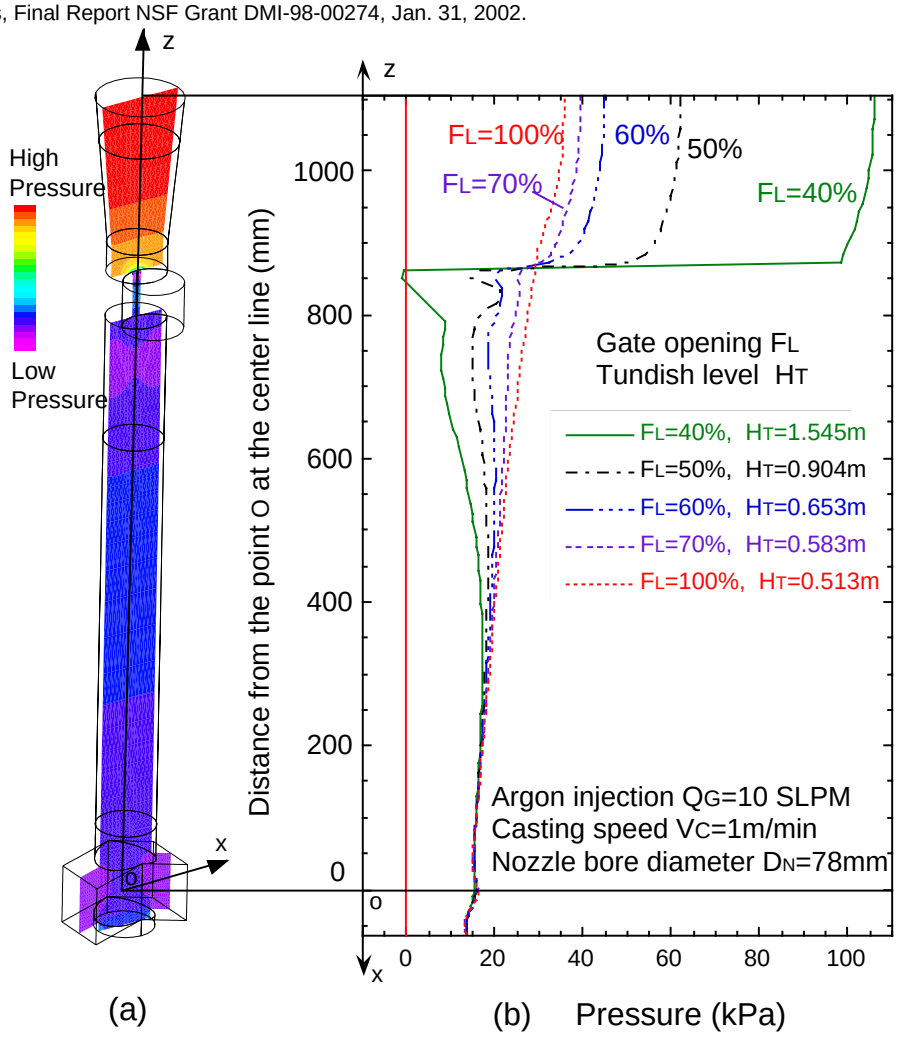

Fig. 5. Pressure drop calculated down nozzle

a) Pressure contours in centerplane showing that major variations are in vertical direction

b) Effect of slide gate opening on vertical pressure distribution

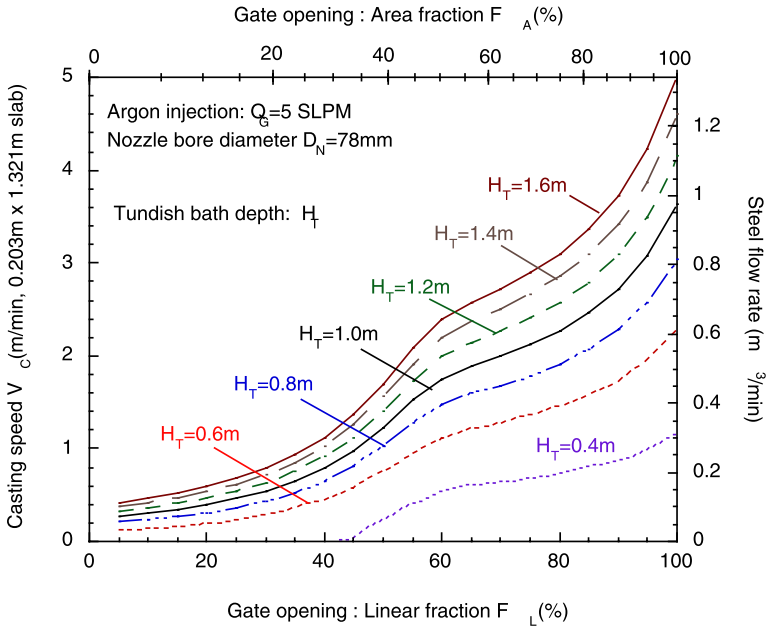

Fig. 6. Effect of slide gate opening size and tundish depth on steel flow rate

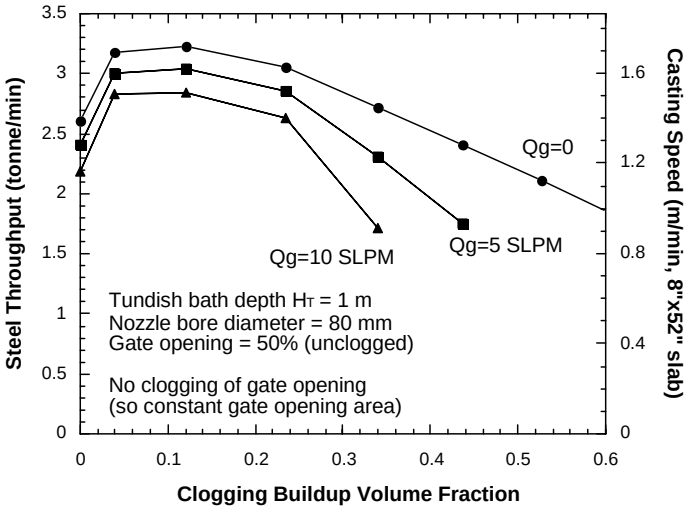

Fig. 7. Effect of clogging buildup on steel throughput (assuming constant gate opening area)

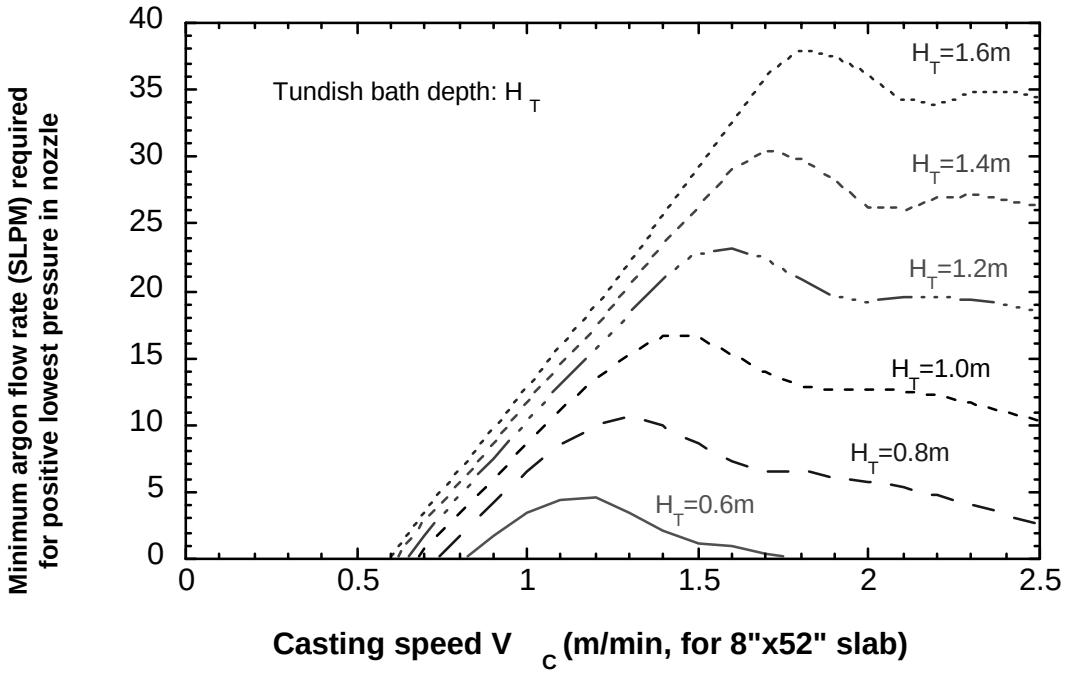

Fig. 8. Optimizing gas injection for different casting speeds and tundish depths

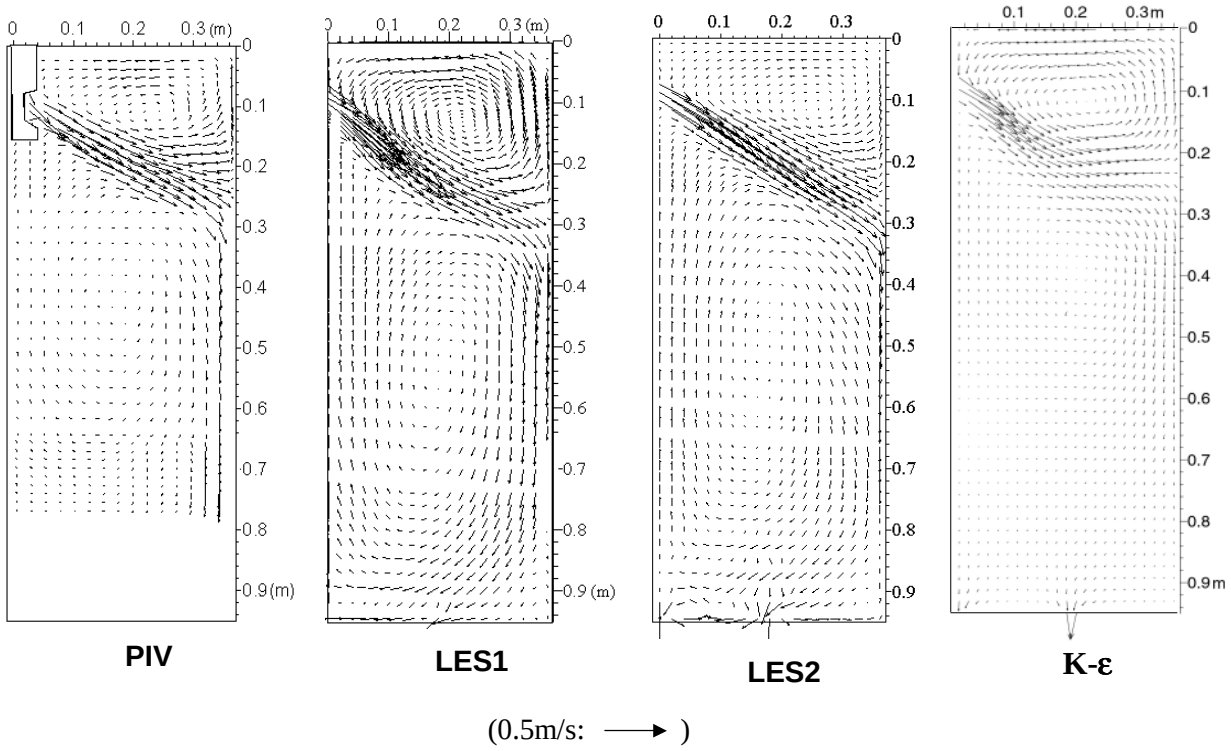

Fig. 9: Comparison of time-average flow pattern in mold centerplane from 4 methods.

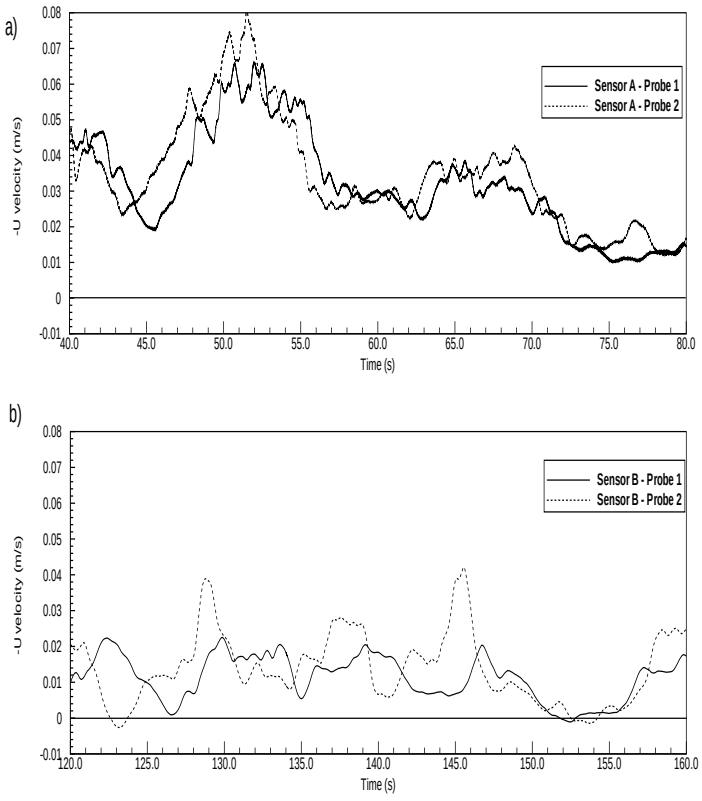

Fig. 10. LES-Simulated electromagnetic probe signals at locations A (a) and B (b).

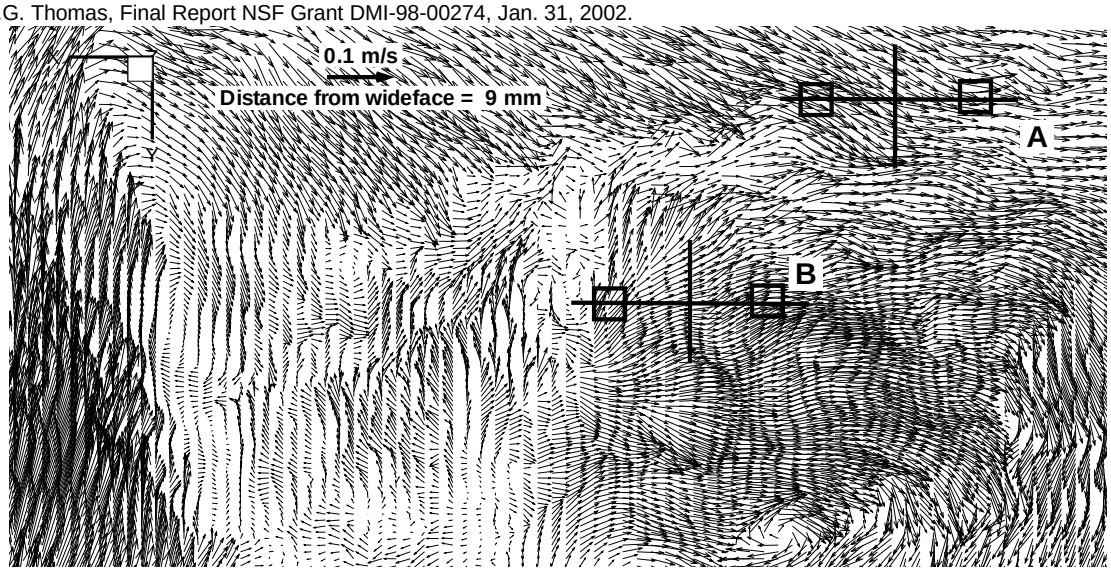

Fig. 11(a). Instantaneous LES-simulated vector plot of the upper roll 9mm from wideface

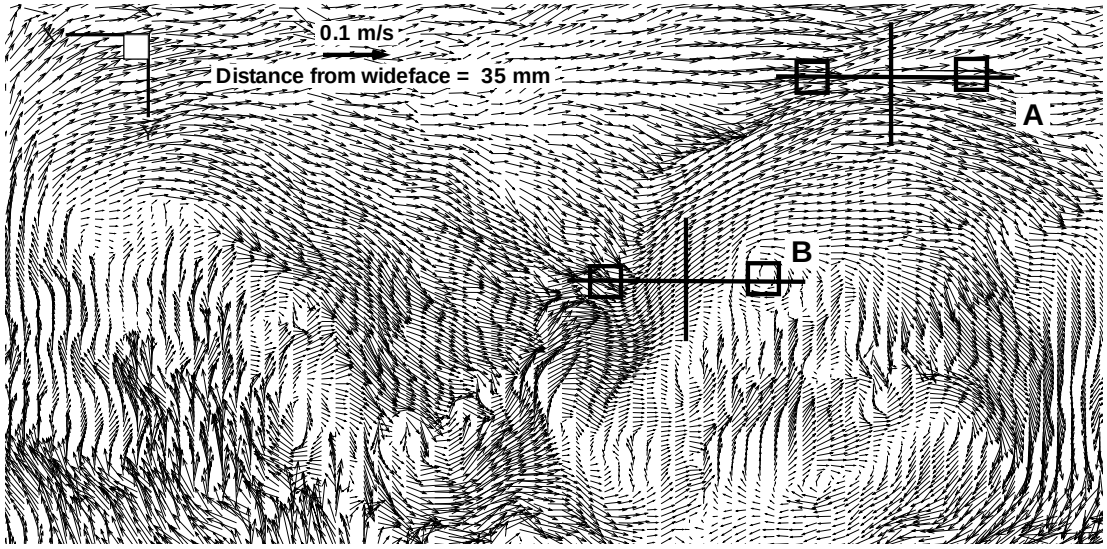

Fig. 11(b). Instantaneous LES-simulated vector plot of the upper roll 35mm from wideface

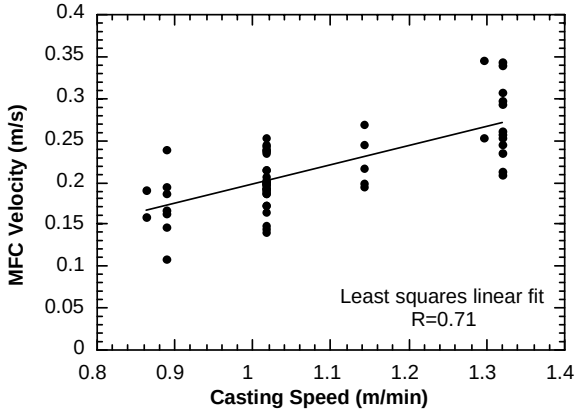

Fig. 12. Electromagnetic sensor output sorted by casting speed

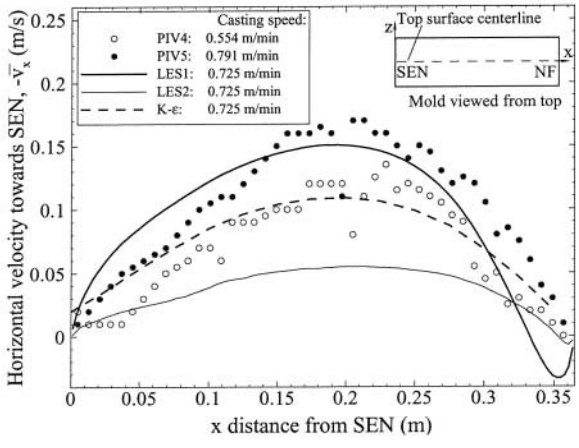

Fig. 13. Time-average speed profile along top surface comparing PIV, K-□, and LES

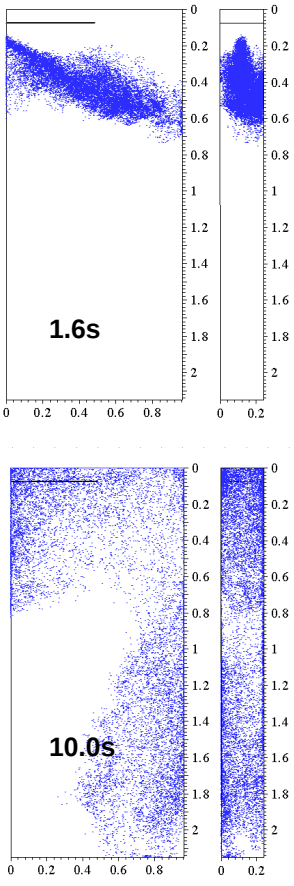

Fig. 14: Distribution of the 15000 particles at four instants after their injection.

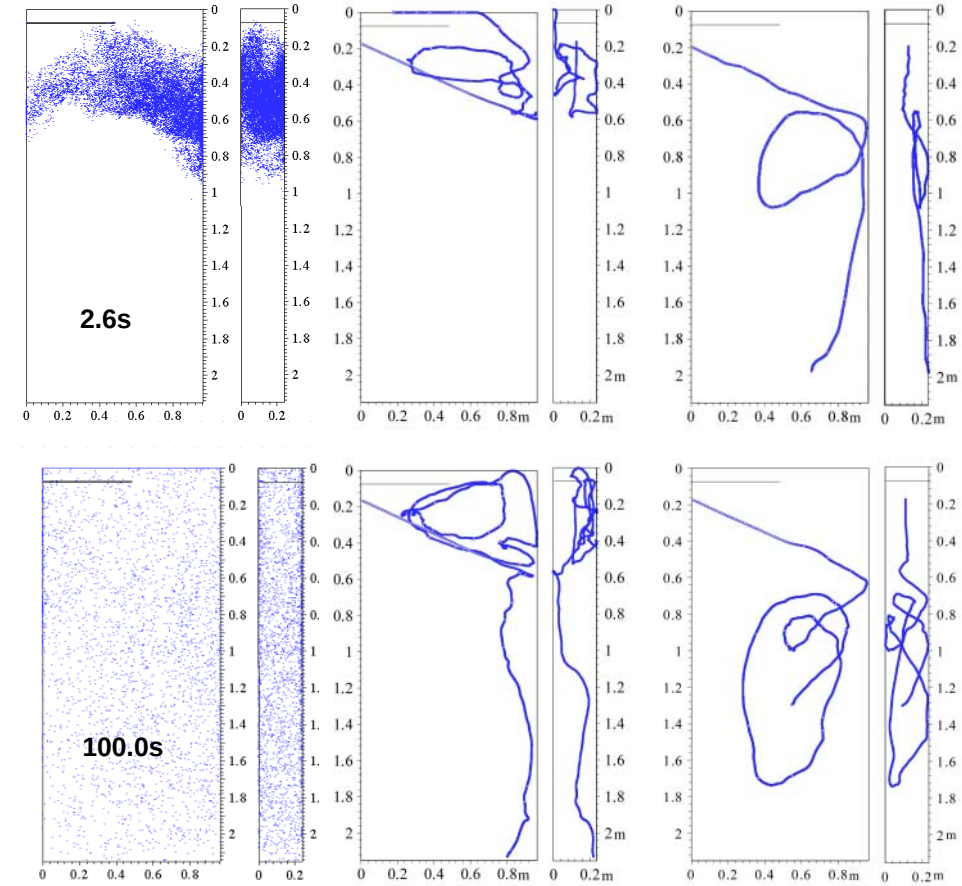

Fig. 15: Four typical particle trajectories found in the computation.

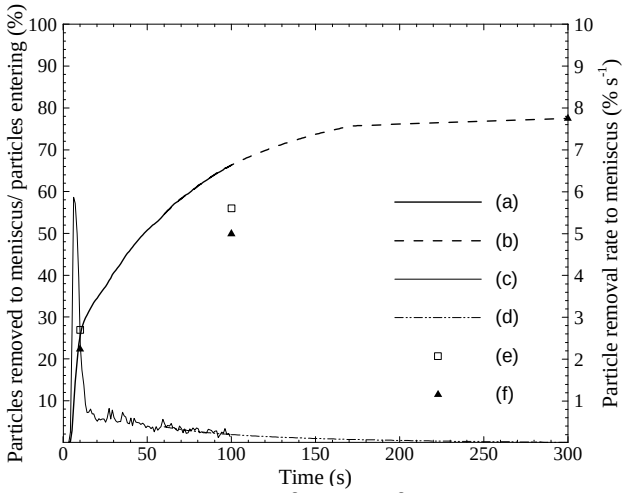

Fig. 16: Particle removal to the top surface in full-scale water model: (a) particles removed to top surface (simulated); (b) particles removed to top surface; (c) particle removal rate to top surface; (d) particle removal rate to top surface; (e) particles removed by screen (LES); (f) particles removed by screen (experiment).

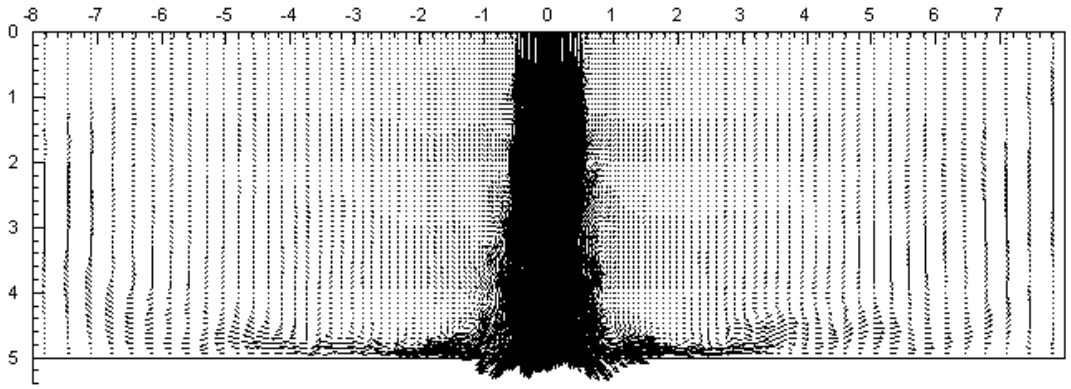

Fig. 17: Instantaneous velocity field.

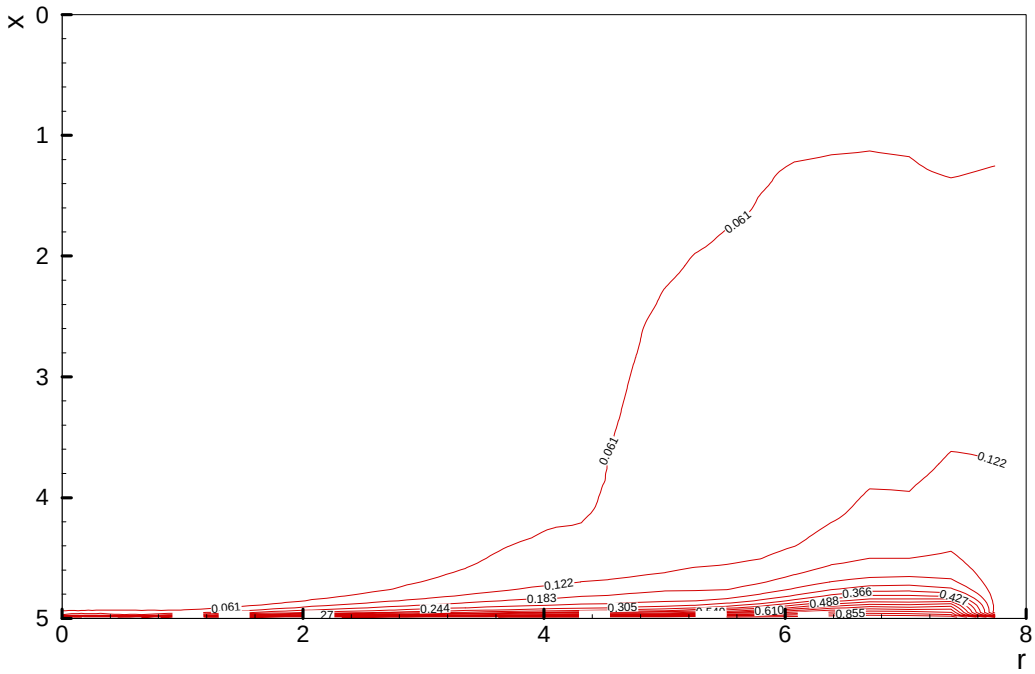

Fig. 18. Time-averaged temperature contours (Re=5,000 from 50k-100k time steps)

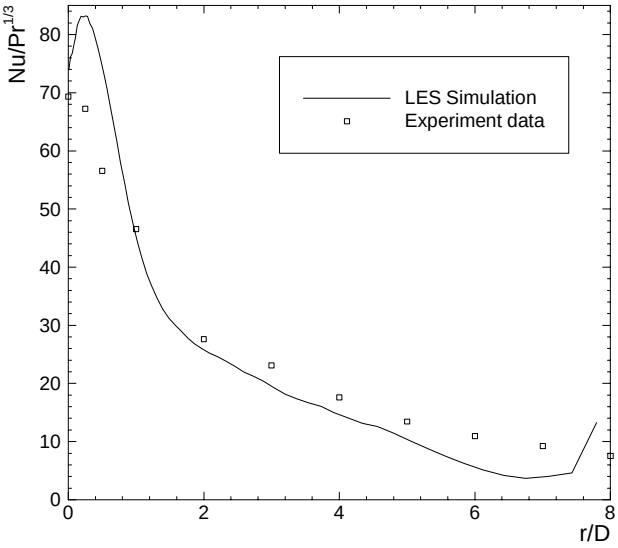

Fig. 19: Time-Mean Dimensionless Heat Transfer Rate.

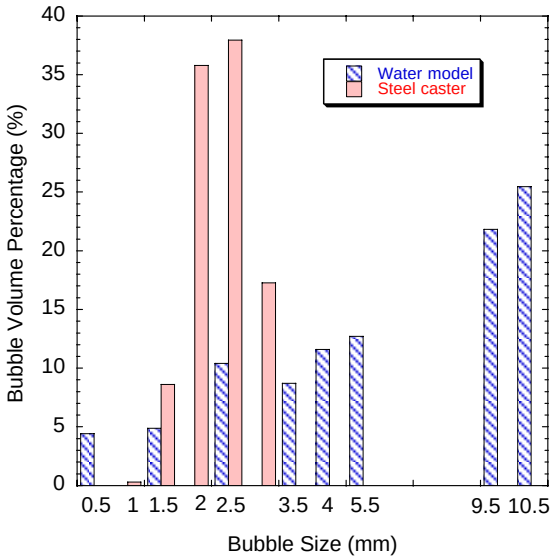

Fig. 20: Bubble distributions entering water model and steel caster.

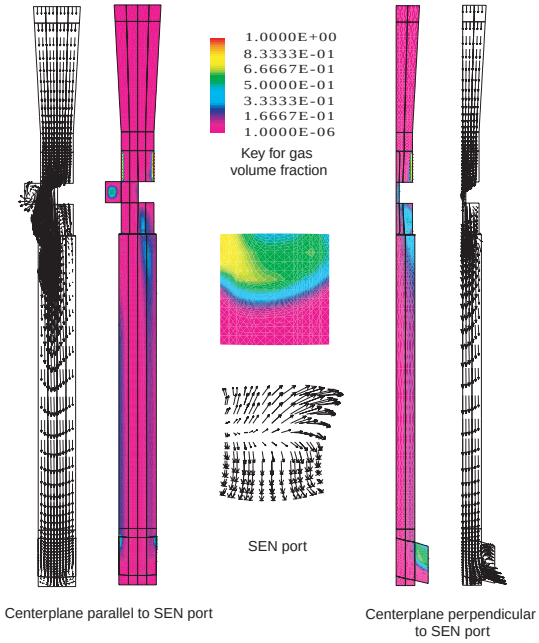

Fig. 21: Computed steel velocity and gas volume fraction in nozzle.

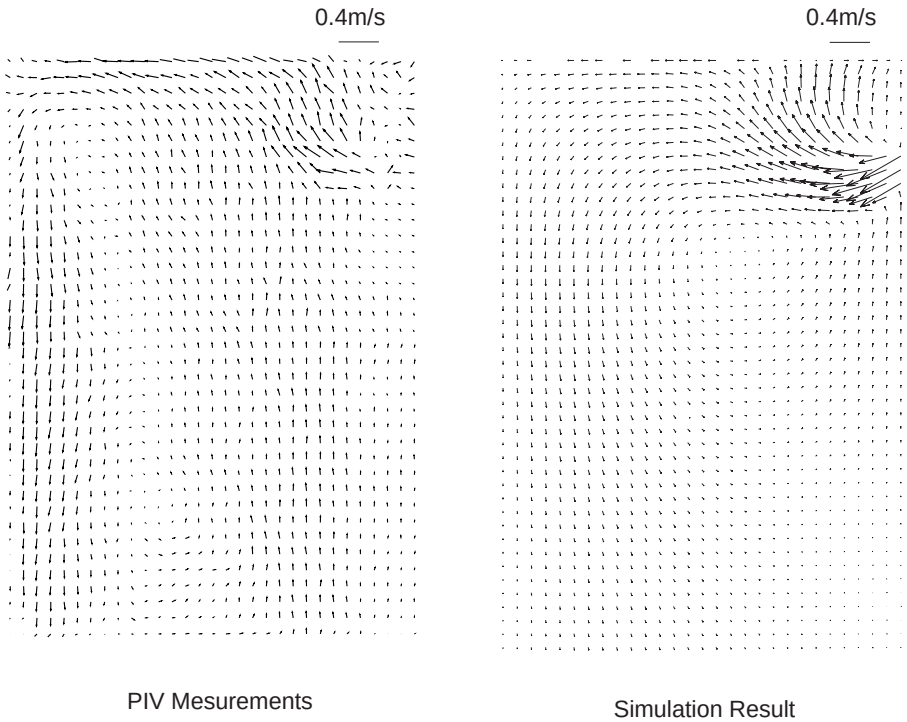

Fig. 22: PIV measurements and computed velocity vectors of multiphase flow in 0.4-scale water model centerplane (Table 3 conditions).

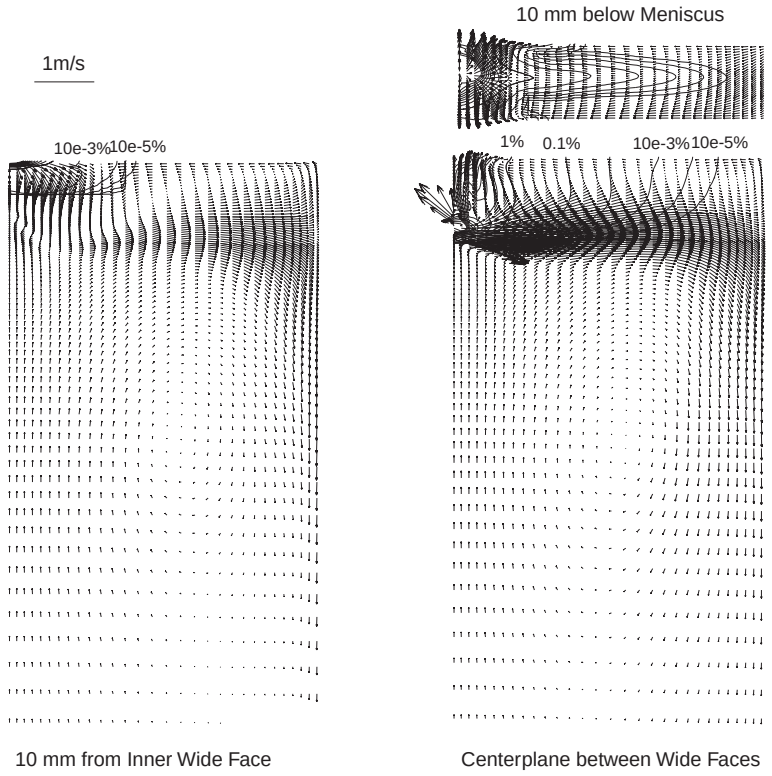

Fig. 23: Computed velocities in steel caster.

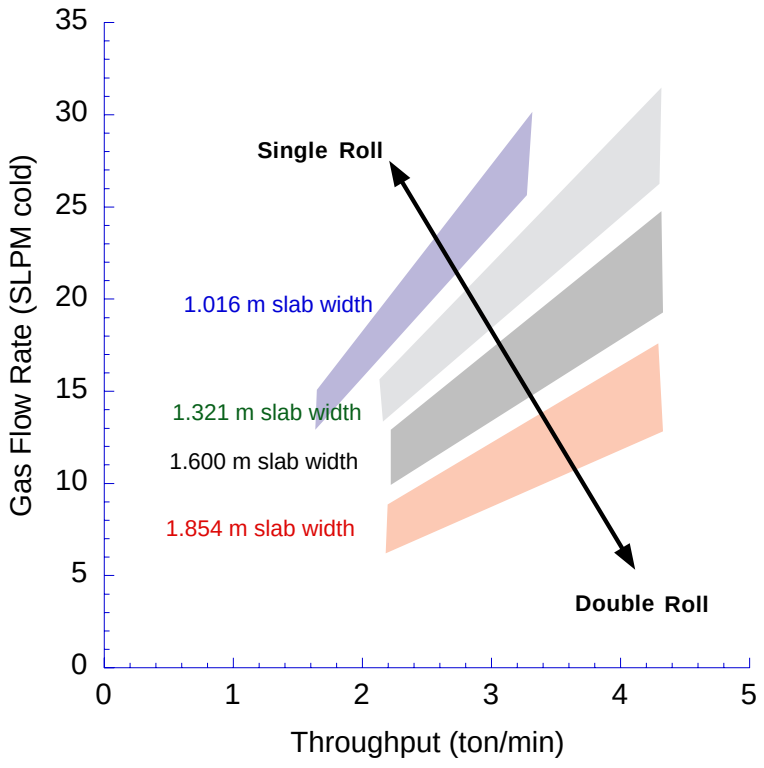

Fig. 24: Effect of casting speed (throughput, slab width, and argon injection rate on mold flow pattern, showing detrimental transition region (shaded boxes)